
ORIGINAL ARTICLE

Customizable wave tailoring materials enabled by coupling nonlinear inverse design at two scales

Brianna MacNider^{1*} | Haning Xiu^{1*} | Kai Qian¹ | Ian Frankel¹ | Hyunsun Alicia Kim^{2,3} | Nicholas Boechler^{1,3}

¹Department of Mechanical and Aerospace Engineering, University of California, San Diego, La Jolla, CA 92093,US

²Department of Structural Engineering, University of California, San Diego, La Jolla, CA 92093,US

³Program in Materials Science and Engineering, University of California, San Diego, La Jolla, CA 92093, US

Correspondence

Nicholas Boechler, Department of Mechanical and Aerospace Engineering, University of California, San Diego, La Jolla, CA 92093,US
Email: nboechler@ucsd.edu

Funding information

UC National Laboratory Fees Research Program of the University of California, Grant Number L22CR4520.

Passive transformation of waves via nonlinear systems is ubiquitous in settings ranging from acoustics to optics and electromagnetics. Passivity is of particular importance for responding rapidly to stimuli, and nonlinearity enormously expands signal transformability compared to linear systems due to the breaking of superposition. It is well known that different types of nonlinearity yield vastly and qualitatively different effects on propagating signals, which raises the question of “what precise nonlinearity is the best for a given wave tailoring application?” This question has largely remained in the regime of simulation and theory, as, until recently it has not been possible to freely choose any optimal nonlinearity (instead relying on limited tunability around known nonlinear mechanisms). Herein, we leverage recent advances in mechanics, wherein desired nonlinear constitutive responses can be achieved through shape optimization, and couple this to a larger-scale, reduced-order nonlinear dynamical inverse design step. Using minimization of kinetic energy transmission from impact as a case study, we identify ideal nonlinear constitutive responses and the geometries needed to achieve them within a single design process. As part of this, we show the large sensitivity of this metric to small

* Equally contributing authors.

changes in nonlinearity, and thus the need for high precision, free-form nonlinearity tailoring. We validate our predictions using impact experiments in a chain of nonlinear springs and masses. This work sets the foundation for broader passive nonlinear mechanical wave tailoring material design, including future incorporation of higher-dimensionality, irreversibility, material heterogeneity, and coupled physics. Potential applications include mechanical computing, acoustic signal and image processing, impact and vibration mitigation, and materials that autonomously respond and conduct directed work via rapid shape-change.

KEYWORDS

inverse design, nonlinear dynamics, nonlinear mechanics, impact mitigation, nonlinear waves

1 | INTRODUCTION

The passive transformation of waves via nonlinear material response is widely used in physical settings ranging from acoustics [1] to optics [2–4] and electromagnetics [5, 6]. Applications include areas such as efficient information transfer [7, 8], computing and logic [9, 10], energy conversion [11], imaging [12], encryption [13], impact and vibration mitigation [14, 15], and rapid shape change [16]. Within these contexts, in contrast to active control, passivity is of particular importance for responding fast to stimuli, and nonlinearity enormously expands signal transformability compared to linear systems due to the breaking of superposition. Indeed, it is well known that different types of nonlinearity yield vastly and qualitatively different effects on propagating signals [17], which raises the question of “what precise nonlinearity is the best for a given wave tailoring application?” This question has largely remained in the regime of simulation and theory, as, until recently, it has not been possible to freely realize any optimal nonlinear constitutive law in practice. The field of mechanics has come furthest towards this goal, by introducing complex, sub-wavelength, geometric motifs to create “mesostructured” nonlinear materials [1], however any tunability seen has been limited around a handful of known nonlinear mechanisms. For instance, broad classes of nonlinearity that have seen tailorability for wave manipulation include contact nonlinearities [18], tensegrity structures [19], and bistable beam arrays [20], among others.

Recent progress has enabled a, thus far unique-to-mechanics, capacity to create materials with on-demand quasi-static nonlinear properties via shape and structural optimization [21–28]. This has included several approaches, including gradient based topology optimization in pursuit of tailoring the entirety of a nonlinear force-displacement curve [21–23] as well as the incorporation of machine learning (ML) algorithms in an attempt to traverse the design space and speed up predictions of mechanical behavior [24, 26–29]. However, such methods alone cannot identify material designs for optimal system-level nonlinear wave tailoring performance. Prior studies of optimal nonlinear dynamic material behavior have tailored heterogeneity with fixed nonlinearity [30], or dynamic behavior where the characteristic wavelengths are on par with or greater than the system size (and thus the response is not “wave-dominated”) and the tailoring was confined to broad metrics like “area under the curve” [31, 32] or “plateau-like” behavior [33].

The role of waves is of particular importance, as allowing for spatiotemporal evolution in nonlinear systems leads to unique emergent phenomena such as solitons [34]. The role of precisely engineered nonlinearities is further important for wave propagation in that seemingly subtle differences in nonlinearity yield *qualitatively* different dynamical behavior. For one example, consider a material with polynomial nonlinearity and all positive coefficients, resulting in a “stiffening” nonlinearity: just small changes in the ratio of coefficients dictate whether or not the system experiences modulational instability [35, 36], or the difference of a quadratic versus cubic perturbation on a linear stiffness results in qualitatively different waveforms and wave mixing behavior [2]. Connecting the inverse design of nonlinear wave response to the quasi-static design of nonlinear constitutive response induced by mesostructure geometry is a significant, and hitherto unsurmounted challenge. If trying to directly extend quasi-static geometric design algorithms based on finite element method (FEM) simulation [21–28] the challenge becomes evident, in that one would need to take the same design variables, copy the geometry over many unit cells, and simulate the entire system in time at high temporal resolution (due to nonlinear generation of high frequency content), and wrap that in an automated design loop—resulting in a task of extreme computational expense.

In this work, we introduce a method to create customizable wave tailoring materials by coupling nonlinear response inverse design at two scales. Namely, we optimize for the emergent dynamic response of the bulk system using a reduced order, discrete element model (DEM) simulation to identify an optimal nonlinear constitutive law for the given performance metric, and couple this to a unit-cell-scale, geometrically-nonlinear, free-form, shape optimization algorithm which designs a physical system that achieves the nonlinear constitutive property identified by the DEM (outlined in Fig. 1). Further, we demonstrate the clear need for high precision nonlinear response design, wherein the system dynamic performance is shown to be highly sensitive to the nonlinear coefficients of the constitutive law. Herein, we choose the maximum kinetic energy transmitted to the boundary of the system in response to an impact event, normalized by that of an otherwise-identical linear system, as our performance metric. The comparison between the linear and nonlinear response is particularly important, as it isolates the role of nonlinearity from other wave manipulating effects such as dispersion and dissipation. We demonstrate the full inverse design of this superior impact mitigation system, from identification of an ideal nonlinearity, to the design of the unit cell geometry, and experimental validation of the performance. An important feature to note, unlike some prior computational quasi-static nonlinear mechanical design strategies [22, 24, 25, 37], we do not use simplified or reduced order models for our underlying mesostructure design, which enables a broader design space and access to highly precise tailoring of nonlinear responses [23]. While we demonstrate our two-scale inverse design for the case of impact mitigation, we expect such an approach for the previously specified nonlinear wave transformation applications [1, 7–13] within the acoustic, phononic, and mechanical wave settings.

2 | RESULTS

2.1 | Reduced order discrete element model

The DEM (Fig. 1A) simulates the impact of a rigid “impactor” block onto a lattice (chain) with N unit cells and a unit cell length. We represent the chain as lumped masses of mass m , interconnected by massless nonlinear springs and inter-site linear dampers, emulating the behavior of a viscoelastic material. The normalized force-displacement relationship for a unit cell of the material is modeled using an up-to third-order polynomial (denoted in Fig. 1B), expressed as $f(x) = x + c_2x^2 + c_3x^3$ (where the force is normalized the linear stiffness c_1^* and $x < 0$ denotes compression, with x the extension of the spring normalized by a). In tension, the response is set to that of a linear spring, such that

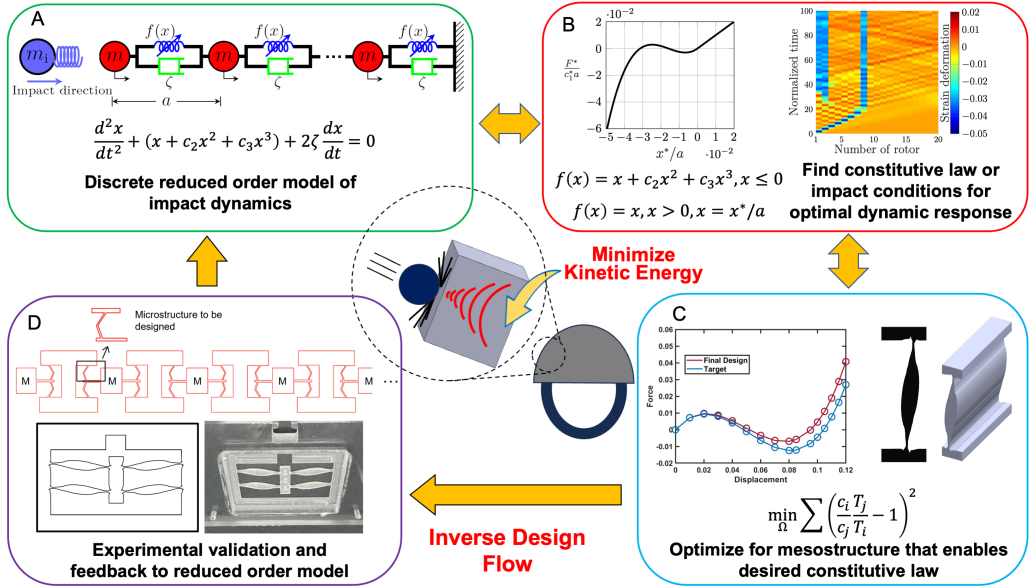


FIGURE 1 Overview of the multilevel design flow. (A) Discrete element model (DEM) simulation of the entire system dynamics. (B) Identification of the optimal nonlinear constitutive law. (C) Shape optimization of a mesostructure to match the identified nonlinear constitutive law. (D) Mechanical and dynamic experimental system characterization.

$f(x) = x$. Incorporating the nonlinear spring into dimensionless equations of motion of the chain we obtain

$$\ddot{x}_i - (x_{i+1} - x_i) + c_2(x_{i+1} - x_i)^2 - c_3(x_{i+1} - x_i)^3 + (x_i - x_{i-1}) - c_2(x_i - x_{i-1})^2 + c_3(x_i - x_{i-1})^3 + 2\zeta(-\dot{x}_{i+1} + 2\dot{x}_i - \dot{x}_{i-1}) = 0, \quad (1)$$

where ζ is the inter-site damping ratio and x_i is the displacement of the i th particle. A variable mass and velocity rigid impactor is used on the left, and a fixed boundary is used on the right. The model also incorporates a contact spring designed to facilitate the smooth contact and controlled release of the impactor during initial impact and rebound, respectively. The simulated dynamical response is acquired through the numerical integration of Eq. (1) via a Runge-Kutta algorithm. The non-dimensionalization of all variables and full details concerning the equations of motion are described in SI Note 1.

2.2 | Optimization of nonlinear constitutive law based on dynamical response

Before searching for optimal nonlinear constitutive responses with our DEM, we set several bounds. First, we confine the unit cell strain to 1 in compression, and set $c_3 > 0$ for simplicity. Second, we restrict our search range for nonlinear coefficients c_2 and c_3 to ensure positive strain energy throughout the entire compression range. By examining the polynomial's properties within this range, we classify the quasi-static response into three distinct zones, "bistability", "monotonic increase", and "local maximum", as shown in Fig. 2A. Bistability (magenta area) denotes the existence of both a local maximum and minimum other than the boundaries (the local minimum does not need to fall below zero). Monotonic increase (blue area) denotes the absence of extrema. Local maximum (green area) signifies the presence

of a local maximum (no local minimum existed) within the range of the length of one unit cell (more details in SI Note 2).

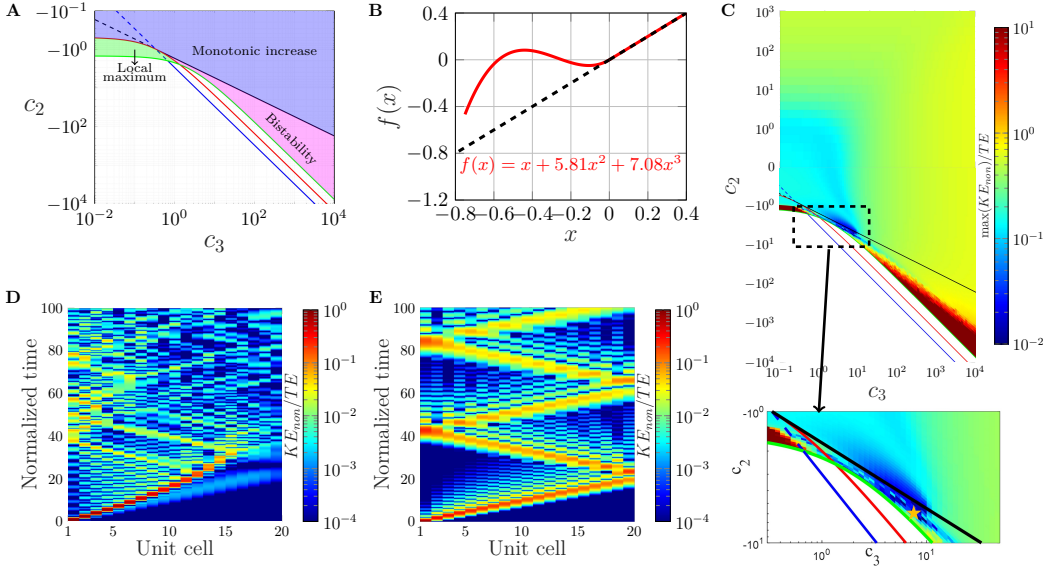


FIGURE 2 Identification of optimal nonlinear constitutive response via DEM simulation for a single impact condition. (A) Feasible solutions of nonlinear spring coefficients c_2 and c_3 . The black line represents $c_2 = -\sqrt{3c_3}$, the red line indicates $c_2 = -(1 + 3c_3)/2$, the blue line is $c_2 = -3c_3$, and the green line is the zero strain energy throughout the whole range, $c_2 = -3/2 - 3c_3/4$. (B) Non-dimensional force displacement relationship of the best performance of the nonlinear spring. (C) Ratio of maximum kinetic energy at the last particle in the nonlinear chain to the initial impact energy as a function of nonlinear spring coefficients for the impact condition of $M/M_0 = 0.05$ and $V/V_0 = 1$, as well as $\zeta = 0.01$. The lines from (A) are overlaid, and the star marker denotes the point of best performance. Normalized kinetic energy of the (D) best performing nonlinear and (E) linear material.

Within these bounds, we first optimize for a singular impact condition ($M/M_0 = 0.05$ and $V/V_0 = 1$), where M_0 is half the mass of the chain and V_0 is the linear sound speed. The material is composed of 20 particles and $\zeta = 0.01$. We vary the nonlinear coefficients of the springs c_2 and c_3 , aiming to minimize the maximum kinetic energy experienced at the end of the material (KE_{non}) normalized by that of a linear system (KE_{lin}) which has all of the same properties except $c_2 = c_3 = 0$. Figure 2C quantifies the ratio of maximum kinetic energy at the end of the material to the initial impact energy (TE), as a function of the coefficients of the nonlinear spring. Around the region of best performance in Fig. 2C ($f(x) = x + 5.81x^2 + 7.08x^3$, plotted in Fig. 2B, and denoted by the star marker in the inset of Fig. 2C) significant performance sensitivity to the constituent nonlinear parameters can be seen (see the zoomed-in view in Fig. 2C). To describe this sensitivity more quantitatively, in SI Note 3 we calculate the gradient of the inset in Fig. 2C, which shows $\partial(KE_{non}/TE)/\partial c_2$ and $\partial(KE_{non}/TE)/\partial c_3$ approaching ± 2 . Spatiotemporal responses of kinetic energy of the optimal nonlinear and linear chain are shown in Fig. 2(D) and (E), respectively. While both materials exhibit an initially sharp pulse, energy from the optimal nonlinear material is trapped around particle 15, preventing further transmission.

In the subsequent analysis, we conduct an optimization wherein we look for optimal nonlinear coefficients for varied impactor mass and velocities. We use the same ratio of the maximum KE of the last particle of the nonlinear

material normalized by that of the linear material as a performance metric (denoted henceforth as “ KE ratio”), wherein a lower ratio indicates superior performance of the nonlinear material. The optimal (minimum) KE ratios with respect to M/M_0 and V/V_0 and corresponding nonlinear spring parameters c_2 and c_3 can be seen in Fig. 3. In contrast to Fig. 2, we use a lower damping ($\zeta = 0.005$), chosen to emulate that of the polycarbonate springs used in our experimental realization. Additional simulation results of KE ratios for increased damping and greater discreteness (more unit cells) are available in SI Note 4 and indicate the potential for KE ratio $< 10^{-2}$ in the latter case. The damping value used in Fig. 3 was chosen to approximate damping found by measuring the resonance of a single connector and nonlinear spring unit (see SI Note 5). Simulation cases of the nonlinear material where self-contact occurs are discarded from consideration of the optimal performance.

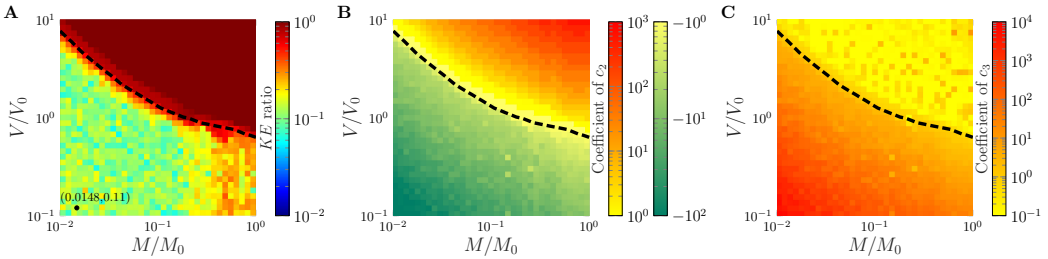


FIGURE 3 Identification of optimal nonlinear coefficients via DEM simulation for varied impactor conditions. (A) Optimal kinetic energy ratio (KE ratio) as a function of impactor conditions and corresponding nonlinear spring coefficients (B) c_2 and (C) c_3 for a material of $N = 20$ and $\zeta = 0.005$. The color bar in (A) is saturated at a KE ratio of unity. The dashed black line denotes the onset of self contact ($x < -1$) in the linear system. The dot in (A) denotes the high performing case used for mesostructure design.

There is a clear boundary where the nonlinear chain does not outperform the linear, which is correlated with the occurrence of self-contact within the linear chain (dashed black line in Fig. 3). At impactor velocities and masses below this threshold, the nonlinear materials exhibit significantly enhanced mitigation effectiveness. As can be seen in Fig. 3A, at a relatively low to moderate level of impactor mass (~ 0.01 to $0.2M_0$), optimal nonlinear materials exhibit a mitigation capability (KE ratio) that is over ten times better than the linear material. As the impactor mass and velocity increase and cross over the dashed black line (orange to red area near the dashed line in Fig. 3A), the priority shifts to preventing contact between unit cells, leading to a comparatively impaired energy-absorbing performance. In future studies, such self contact could be explored as a form of nonlinearity and design feature, instead of a constraint.

A specific optimal solution (pair of coefficient ratios) was chosen from a set of multiple solutions showing high performance KE ratio. We further downselected, looking for a solution also with relatively low strain, making it more amenable to experimental implementation. The chosen solution is a nondimensional nonlinear mechanical response of the form $f(x) = x + 94.4x^2 + 2000x^3$ in compression, with an impact condition of $M/M_0 = 0.0148$ and $V/V_0 = 0.11$ (marked in Fig. 3A). This nonlinear constitutive law is used as the target for the mesostructure design, with the goal of finding a geometry that yields that nonlinear mechanical response.

2.3 | Shape optimization for desired nonlinear constitutive law

In order to find a spring geometry that gives the desired nonlinear response, a two-dimensional shape optimization approach is taken, using a level-set optimization method [23]. A third order polynomial is fit to the calculated force-

displacement behavior of the structure, and the objective of the optimization problem is taken as the ratio of nonlinear to linear terms. The exact form of the objective function is

$$\min_{\Omega} \sum \left(\frac{c_i}{c_j} \frac{T_j}{T_i} - 1 \right)^2, \quad (2)$$

where c_i and c_j represent the current polynomial coefficients, and T_i and T_j represent the target coefficients. By taking the ratio of the polynomial terms, the nonlinearity of the structure is decoupled from the linear stiffness, allowing the optimizer more design freedom, leading to more robust convergence. To further aid in the navigation of the design space, we select an initial condition for our optimization process which displays qualitatively similar behavior to that desired (see SI note 5).

When realizing our nonlinear chain we employ comparatively rigid frames around the designed spring to mimic fixed boundary conditions (as can be seen in Fig. 1D) and rigid connectors between the springs to allow relative movement of the particles. With the addition of these components we have a unit cell length, a , and a nonlinear spring design domain length that encompasses only a portion of this larger unit cell. We call this portion of a the spring length, and denote it by a_s (and, hereafter, the subscript s is used to refer to parameters defined on the scale of the spring). Figure 4E highlights the difference between these two length scales. Because the DEM-identified polynomial constitutive law is expressed as a function of strain, and the strain experienced by the spring across a_s is different than that experienced by the entire unit cell across a for a fixed applied displacement, the targeted polynomial is therefore scaled accordingly. We take the ratio of nonlinear terms as $R = (c_i \epsilon^i) / (c_1 \epsilon)$ and $R_s = (c_{s,i} \epsilon_s^i) / (c_{s,1} \epsilon_s)$ on the scales of a and a_s , respectively, with i representing the order (or power) of the term and ϵ representing the maximum strain experienced on the corresponding length scale. In order for equivalent degrees of nonlinearity to be displayed at different scales, we take $R = R_s$ at the maximum strain considered in each scale, and solve for updated c_i or $c_{s,i}$ terms.

The optimization target (recall, on the unit cell scale, identified above as $f(x) = x + 94.4x^2 + 2000x^3$) can therefore be expressed on the spring length scale as $f = x_s - 30.2x_s^2 + 204.8x_s^3$, by setting $R = R_s$ and solving for $c_{s,i}$. The final optimized structure, shown in Fig. 4A-B, achieved an experimental force-displacement law on the spring scale of $f(x) = -0.0003 + x_s - 28.28x_s^2 + 193.13x_s^3$, resulting in a percent difference between targeted and obtained polynomial ratios of 5.70% for the third order ratio and 6.34% for the second order ratio.

As the multilevel optimization methodology is a loop in which inputs from the DEM and shape optimization feed back into one another, the design process can be followed in either direction, which can be exploited for exploration of the space. For example, while one may begin with a desired impact condition which is then fed into the DEM simulation followed by the mesostructure optimization, one might just as easily begin with some nonlinearity and feed this into the DEM simulation to explore what impact conditions it might perform well (or poorly) for. Similarly, one might find that the physical design domain requires constraints, or that optimized structures exhibit structural damping which diverges significantly from predictions, and these updated considerations can be flowed back up to the DEM simulation to search for the updated optimum conditions.

In the example shown herein, we strive for generality, thus there was no single impact condition specified. The solutions were chosen which exhibited low impactor mass and velocity, as well as low maximum strain, in order to avoid the onset of plasticity in the fabricated structures. One can just as well begin with a strict impact condition requirement, and flow through the multilevel optimization methodology accordingly. If larger mass and velocity, and therefore larger strains, are desired, the mesostructure optimization portion can be undertaken with a Neo-Hookean material model, and the real-world structures fabricated out of some soft, flexible material, such as silicone (see Ref.

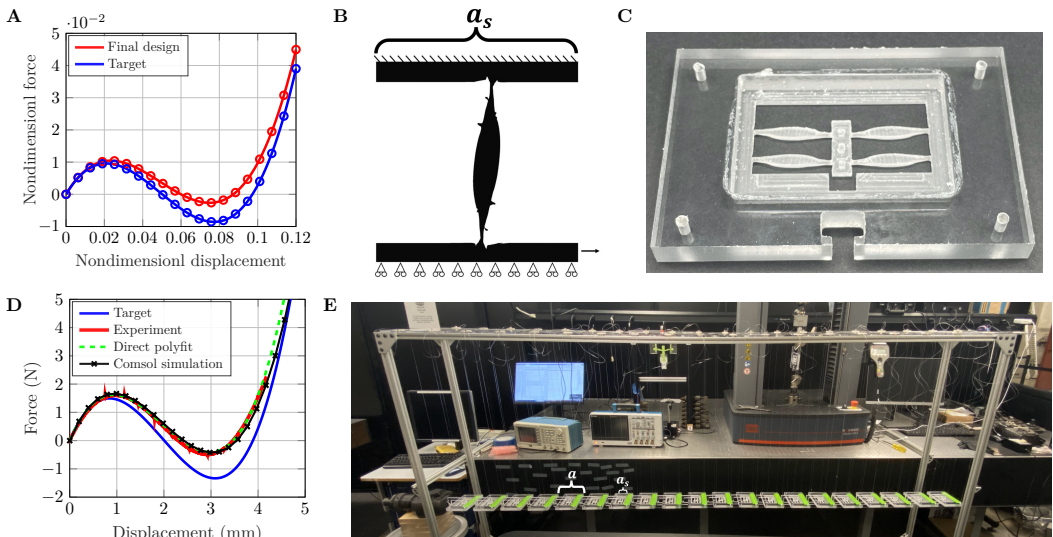


FIGURE 4 Shape optimization to identify geometry giving DEM identified desired constitutive law, and experimental realization of the spring and chain. A-B) Results of the shape optimization, with the target and final force-displacement curves shown in (A), and the optimized design shown in (B). C) The fabricated polycarbonate unit cell, consisting of four optimized springs (as seen in (B)) and a rigid frame to impose boundary conditions. D) The quasi-static test of the unit cell shown in (C), compared against the behavior of a single spring with perfectly imposed boundary conditions as simulated via Comsol FEM simulation. E) The full chain of 20 unit cells, hung from a frame. The chain is clamped to the left of the leftmost unit cell, imposing a zero displacement boundary condition. The impact occurs at the right end of the chain. The unit cell and spring length scales are labeled.

[23]).

2.4 | Experimental validation

In our experimental realization of the chains, the spring scale $a_s = 40$ mm was chosen and incorporated into the rigid frame and connector, resulting in a unit cell length $a = 125$ mm. In order to minimize the non-longitudinal motion of the masses, a second nonlinear spring was added in parallel to the first. A single unit cell (shown in Fig. 4C) was fabricated by cutting the shape out of a polycarbonate sheet via computer-numerical-control (CNC) milling. We note the design of the frame surrounding a spring is particularly important in properly imposing boundary conditions, and thus critical in matching simulation predicted force displacement curves. This single unit cell was tested quasi-statically to confirm the performance of the spring, as shown in Fig. 4D. Repeated, cyclic quasi-static loading tests were performed to confirm that no onset of plasticity or fatigue occurs during the dynamic experiment (see SI Note 5).

A chain of twenty unit cells was fabricated and hung from a frame in order to minimize friction, as shown in Fig. 4E. Stationary rails (not pictured in Fig. 4E) were positioned on either side of the hanging masses to minimize lateral motion, with care taken to position the rails such that contact with the hanging masses was nonexistent at rest. Impact tests were undertaken where the mass and velocity of the impactor were chosen based upon the optimal conditions identified in the DEM results, in the case with an impactor mass of $M = 20$ g and a velocity of $V = 2$ m/s. Data was collected through the use of several cameras positioned along the length of the chain, allowing digital image

processing to be used to track the impact wave across the length of the system. In addition, a laser Doppler vibrometer (see SI Note 6) was pointed at the last unit cell in the system, allowing for the second measurement of the velocity of the last unit cell. Impact tests were repeated several times. A similar chain of twenty linear unit cells, with similar linear stiffness and mass (the mass of the linear and nonlinear unit cells are 152.5 g and 152.8 g, respectively) values, was then constructed to act as a control for comparison against the nonlinear chain (see SI Note 6 for more details), and the impact tests were repeated. It is noted that for the kinetic energy transmission ratio considered herein, the magnitude of the linear stiffness (even if different between the linear and nonlinear chain) does not matter (see SI Note 7).

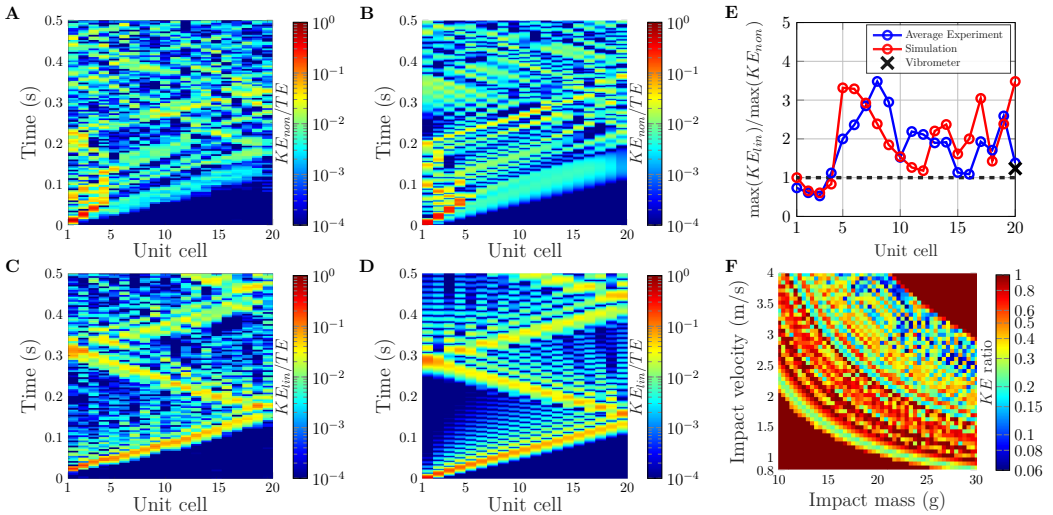


FIGURE 5 Experimental validation of the optimal nonlinear and linear chains, compared with simulation predictions. A-D) Spatiotemporal evolution of kinetic energy in the system (normalized by the input kinetic energy, or initial total energy). The nonlinear chain is shown in A (experiment, nonlinear trial 1) and B (simulation), while the linear case is shown in C (experiment, linear trial 1) and D (simulation). The experimental spatiotemporal plots include a smoothing of displacement values to assist with noise induced by differentiating the discrete time camera data. The spatiotemporal plots for other trials are included in SI Note 6. E) The maximum kinetic energy (linear/nonlinear) seen at each unit cell for both experiment and simulation. A value greater than 1 indicates superior performance of the nonlinear chain as compared to the linear. The experiment values are the average taken from three experimental trials. The X marks the average experimental value recorded by the vibrometer (see SI Note 6 for the full data sets), which collected data from only the last unit cell. F) The simulated sensitivity of the KE ratio (truncated at 1) to impact conditions, wherein the simulation was run with the coefficients that were found experimentally from the nonlinear spring in Fig. 4D (that is, the physically achieved coefficients).

Several key metrics were examined to confirm the performance of the system, the results of which are summarized in Fig. 5. Foremost among these results is the velocity (or kinetic energy) which was transmitted to the end of the chain. Measured spatiotemporal kinetic energy responses are shown in Fig. 5A-D, in which we can see that the nonlinear cases dissipate and trap kinetic energy through unit cell snapping, preventing much of it from reaching the right (or protected) end of the chain (a large portion of the kinetic energy is seen to remain, reflecting back and forth, in the first 4-5 unit cells in panels A and B). We note an excellent match between simulation (using the experimentally fit coefficients taken from the quasi-static force-displacement curve shown in Fig. 4D) and experiment in these spa-

tiotemporal plots. In particular, as seen in Fig. 5A and B, the number of unit cells that underwent snap-through in the nonlinear chain (four in both simulation and experiment, identified by the high kinetic energy values in unit cells 1-4 which then greatly reduce in subsequent unit cells when snapping is no longer occurring—see also the strain x-t diagrams and the experiment videos included in SI Note 6) also shows excellent agreement. Computational explorations showed this metric to be highly sensitive to small changes in polynomial coefficients and input conditions. Figure 5E shows a comparison of the ratio (of linear to nonlinear cases) of the maximum kinetic energy seen at each unit cell, in both experiment (averaged across three trials—we note that several later trials [See SI Note 6] were excluded from averaging, due to a likely degraded behavior of the spring after multiple tests, slightly adjusted experimental conditions, and potential sensitivity effects as explored further below) and simulation. We observe largely good agreement between the simulation and experiment. We see a larger discrepancy at the last particle (Fig. 5E), which we attribute to non-ideal boundary conditions. A point of particular note, is that although the targeted conditions show excellent predicted performance, the behavior can be sensitive to small variations in impactor mass and velocity (see the simulation data of Fig. 5F). To more quantitatively describe this sensitivity, in SI Note 3, we calculate gradient of Fig. 5F, which shows $|\partial(KE_{ratio})/\partial M| \approx 2$ and $\partial(KE_{ratio})/\partial V \approx 5$. This sensitivity is amplified in the presence of bistability, in which the snapping (or lack thereof) of a single unit cell can push the system from one qualitative behavior well to another (see SI Note 3). The impactor velocities seen herein were not precise (ranging from 2.10–2.19 m/s, see SI Note 6), and this, coupled with the aforementioned sensitivity provides an insight into variations in chain performance—namely, that the slight variations in impactor velocity we see in experiment have the potential to easily knock the system out of its optimal performance region, into one in which poorer performance is to be expected. Despite the sensitivity of the system, per Fig. 5E the kinetic energy ratio (KE_{lin}/KE_{non}) remains greater than 1 (superior performance of the nonlinear chain compared to the linear) for both simulation and experiment once a critical number of unit cells has passed (unit cell 5 for the simulation, unit cell 4 in experiment). Additional tests of the decay rate of a low amplitude propagating pulse in both chains (see SI Note 5) suggest the damping in the linear chain is actually higher than the nonlinear one. This highlights the value of nonlinear wave manipulation, where superior performance can be seen even compared to a linear system with greater damping.

We include here a further discussion on the simulated sensitivity of the performance with respect to the impact conditions plotted in Fig. 5F (the gradients of KE ratio with respect to the mass and velocity are represented in SI Note 3). The variability of the mass-velocity space is immediately apparent, with several very small regions of excellent performance (low KE ratios) surrounded by oscillating regions of lower performance (relatively higher KE ratios), and even several points of poor performance (in which the ratio of nonlinear to linear maximum kinetic energy approaches or exceeds 1). The optimum performance region targeted in this work lies in one of these small low KE ratio regions, and slight deviations in the impactor velocity and mass can therefore be expected to produce variable and poorer nonlinear chain performance. This phenomenon reveals important characteristics regarding the sensitivity of the system, and more generally nonlinear dynamical systems wherein bifurcation can cause sharp changes in behavior [38]. We believe the proximity of regions of poor performance to regions of good performance (e.g. Fig. 5F) motivates a consideration of nearby conditions in future work. For instance, we expect there are application scenarios in which a region of reduced sensitivity to changes in stimuli may be desirable at the expense of slightly lowered performance.

3 | CONCLUSION

In this work, we have demonstrated an integrated, two-level inverse design methodology for nonlinear wave tailoring in a mechanical system. Including the possibility of more highly discretized materials (100 unit cells, see SI Note

4), our optimizations of nonlinear constitutive laws suggest the potential for over two orders of magnitude improvement (reduction) in kinetic energy transmission via the use of a nonlinear material compared to a comparative linear material. Our initial experiments on materials with fewer unit cells (20) show close agreement with our simulations, validating our two-level design approach. We also observed large sensitivity of the kinetic energy transmission metric to small changes in nonlinearity and impact conditions, which we suggest highlights the need for high precision, free-form nonlinearity tailoring, as well as future study of nonlinear dynamical design for robustness-of-response to the presence of defects, disorder, and stimuli variation. Within the considered topic of impact mitigation, a near term question of future interest would be how such optimal nonlinearities would change for a different metric such as maximum transmitted force or peak tensile stress anywhere in the material. Similarly, although our proof of concept study focused on impact, we envision a wide range of applications that could make use of precisely tailored nonlinear signal transformation such as mechanical computing, acoustic signal and image processing, vibration mitigation, and materials that autonomously respond and conduct directed work via rapid shape-change. Additional future research areas include extension of this method to less scale separated dynamical (no lumped masses), higher-dimensional, irreversible constitutive, heterogeneous material, active, and coupled-physics settings.

Acknowledgements

This work was supported by the UC National Laboratory Fees Research Program of the University of California, Grant Number L22CR4520. B.M. acknowledges support from the U.S. Department of Energy (DOE) National Nuclear Security Administration (NNSA) Laboratory Graduate Residency Fellowship (LRGF) under Cooperative Agreement DE-NA0003960. I.F. acknowledges support from the Department of Defense (DoD) through the National Defense Science & Engineering Graduate (NDSEG) Fellowship Program.

Conflict of Interest

The authors declare no conflicts of interest.

References

- [1] Patil GU, Matlack KH. Review of exploiting nonlinearity in phononic materials to enable nonlinear wave responses. *Acta Mechanica* 2022;233(1):1–46.
- [2] Boyd RW. *Nonlinear optics*. 3rd ed. ed. Amsterdam ;: Academic Press; 2008.
- [3] Kauranen M, Zayats AV. Nonlinear plasmonics. *Nature photonics* 2012;6(11):737–748.
- [4] Litchinitser NM. Nonlinear optics in metamaterials. *Advances in Physics: X* 2018;3(1):1367628.
- [5] Lapine M, Shadrivov IV, Kivshar YS. Colloquium: Nonlinear metamaterials. *Rev Mod Phys* 2014 Sep;86:1093–1123.
- [6] Fairbanks AJ, Darr AM, Garner AL. A review of nonlinear transmission line system design. *IEEE Access* 2020;8:148606–148621.
- [7] Wang W, Wang L, Zhang W. Advances in soliton microcomb generation. *Advanced Photonics* 2020;2(3):034001–034001.
- [8] Smirnova D, Leykam D, Chong Y, Kivshar Y. Nonlinear topological photonics. *Applied Physics Reviews* 2020;7(2).

- [9] Marcucci G, Pierangeli D, Conti C. Theory of neuromorphic computing by waves: machine learning by rogue waves, dispersive shocks, and solitons. *Physical Review Letters* 2020;125(9):093901.
- [10] Yasuda H, Buskohl PR, Gillman A, Murphey TD, Stepney S, Vaia RA, et al. Mechanical computing. *Nature* 2021;598(7879):39–48.
- [11] Dmitriev VG, Gurzadyan GG, Nikogosyan DN. *Handbook of nonlinear optical crystals*, vol. 64. Springer; 2013.
- [12] Wang T, Sohoni MM, Wright LG, Stein MM, Ma SY, Onodera T, et al. Image sensing with multilayer nonlinear optical neural networks. *Nature Photonics* 2023;17(5):408–415.
- [13] Zhang YQ, Wang XY. A symmetric image encryption algorithm based on mixed linear–nonlinear coupled map lattice. *Information Sciences* 2014;273:329–351.
- [14] Nesterenko V. *Dynamics of heterogeneous materials*. Springer Science & Business Media; 2013.
- [15] Fancher R, Frankel I, Chin K, Abi Ghanem M, MacNider B, Shannahan LS, et al. Dependence of the kinetic energy absorption capacity of bistable mechanical metamaterials on impactor mass and velocity. *Extreme Mechanics Letters* 2023;p. 102044.
- [16] Jin L, Khajetourian R, Mueller J, Rafsanjani A, Tournat V, Bertoldi K, et al. Guided transition waves in multistable mechanical metamaterials. *Proceedings of the National Academy of Sciences* 2020;117(5):2319–2325.
- [17] Scott A. *Encyclopedia of nonlinear science*. Routledge; 2006.
- [18] Porter MA, Kevrekidis PG, Daraio C. Granular crystals: Nonlinear dynamics meets materials engineering. *Physics Today* 2015;68(11):44–50.
- [19] Fraternali F, Carpentieri G, Amendola A, Skelton RE, Nesterenko VF. Multiscale tunability of solitary wave dynamics in tensegrity metamaterials. *Applied Physics Letters* 2014;105(20):201903.
- [20] Meaud J, Che K. Tuning elastic wave propagation in multistable architected materials. *International Journal of Solids and Structures* 2017;122-123:69–80.
- [21] Li W, Wang F, Sigmund O, Zhang XS. Design of composite structures with programmable elastic responses under finite deformations. *Journal of the Mechanics and Physics of Solids* 2021;151:104356.
- [22] Li W, Wang F, Sigmund O, Zhang XS. Digital synthesis of free-form multimaterial structures for realization of arbitrary programmed mechanical responses. *Proceedings of the National Academy of Sciences* 2022;119(10):e2120563119.
- [23] MacNider B, Frankel I, Qian K, Pozos A, Santos A, Kim HA, et al. Tailoring high precision polynomial architected material constitutive responses via inverse design. *arXiv* 2023;p. 2306.06585.
- [24] Deng B, Zareei A, Ding X, Weaver JC, Rycroft CH, Bertoldi K. Inverse Design of Mechanical Metamaterials with Target Nonlinear Response via a Neural Accelerated Evolution Strategy. *Advanced Materials* 2022;p. 2206238.
- [25] Zheng L, Karapiperis K, Kumar S, Kochmann DM. Unifying the design space and optimizing linear and nonlinear truss metamaterials by generative modeling. *Nature Communications* 2023;14(1):7563.
- [26] Brown NK, Garland AP, Fadel GM, Li G. Deep reinforcement learning for the rapid on-demand design of mechanical metamaterials with targeted nonlinear deformation responses. *Engineering Applications of Artificial Intelligence* 2023;126:106998.
- [27] Ha CS, Yao D, Xu Z, Liu C, Liu H, Elkins D, et al. Rapid inverse design of metamaterials based on prescribed mechanical behavior through machine learning. *Nature Communications* 2023;14(1):5765.

- [28] Bastek JH, Kochmann DM. Inverse design of nonlinear mechanical metamaterials via video denoising diffusion models. *Nature Machine Intelligence* 2023;5(12):1466–1475.
- [29] Zheng X, Zhang X, Chen T, Watanabe I. Deep Learning in Mechanical Metamaterials: From Prediction and Generation to Inverse Design. *Advanced Materials* 2023;p. 2302530.
- [30] Fraternali F, Porter MA, Daraio C. Optimal design of composite granular protectors. *Mechanics of Advanced Materials and Structures* 2009;17(1):1–19.
- [31] Deng H, Cheng L, Liang X, Hayduke D, To AC. Topology optimization for energy dissipation design of lattice structures through snap-through behavior. *Computer Methods in Applied Mechanics and Engineering* 2020;358:112641.
- [32] Chen Q, Zhang X, Zhu B. Design of buckling-induced mechanical metamaterials for energy absorption using topology optimization. *Structural and Multidisciplinary Optimization* 2018;58(4):1395–1410.
- [33] Zeng Q, Duan S, Zhao Z, Wang P, Lei H. Inverse Design of Energy-Absorbing Metamaterials by Topology Optimization. *Advanced Science* 2023;10(4):2204977.
- [34] Dauxois T, Peyrard M. *Physics of Solitons*. Cambridge University Press; 2006. https://books.google.com/books?id=YKe1UZc_Qo8C.
- [35] Boehler N, Theocharis G, Job S, Kevrekidis PG, Porter MA, Daraio C. Discrete breathers in one-dimensional diatomic granular crystals. *Physical review letters* 2010;104(24):244302.
- [36] Huang G, Hu B. Asymmetric gap soliton modes in diatomic lattices with cubic and quartic nonlinearity. *Phys Rev B* 1998 Mar;57:5746–5757. <https://link.aps.org/doi/10.1103/PhysRevB.57.5746>.
- [37] Ha CS, Yao D, Xu Z, Liu C, Liu H, Elkins D, et al. Rapid inverse design of metamaterials based on prescribed mechanical behavior through machine learning. *Nature Communications* 2023;14(1):5765.
- [38] Strogatz SH. *Nonlinear dynamics and chaos: with applications to physics, biology, chemistry, and engineering*. CRC press; 2018.